Study on Electromagnetic Vibration Characteristics of Anode Saturable Reactor Considering Anisotropic Properties

Tao Chen, Qingxin Yang, Changgeng Zhang, Yongjian Li, Yu Dou, and Shuaichao Yue

***Abstract*—The anode saturable reactor (ASR) as a pivotal electrical device is used to protect thyristors working in the converter valve of ultrahigh-voltage direct current (UHVdc) power transmission systems. This article aims to delve into the magnetic and vibration characteristics of the ASR by simulation and experimental measurements. Based on the anisotropic material properties, the vibration numerical model of the ASR core is established by the finite element method. The magnetic–mechanical coupling simulation of the core is calculated and analyzed. To verify the accuracy of the model, the vibration modes and the vibration velocity of the core are measured experimentally by building a measuring platform. The error is less than 10% by comparing the experimental results with the simulation results. The uncertainty of the measurement is analyzed and measures to improve the stability of the measurement results are proposed.**

***Index Terms*—Anode saturable reactor (ASR), electromagnetic vibration, finite element method, grain-oriented silicon steel sheet (GOSSS).**

I. Introduction

DUE to the rapid development of power electronics technology, ultrahigh-voltage direct current (UHVdc) transmission has unique advantages for grid interconnection and long-distance transmission. With the wide application of industrial engineering, the security of power systems needs to be considered further. A series of protective devices, such as the anode saturable reactor (ASR), are used to avoid the influence of large-capacity dynamic reactive power fluctuations on the power grid and electrical equipment, thereby improving power supply quality [1]. The ASR and thyristor are connected in series, which is used to limit the rapid current rise and protect the thyristor in the power grid [2]. Under the complex applied magnetic and mechanical fields, the vibration of ASR is inevitably generated because of the Maxwell stress and magnetostrictive stress originating from the grain-oriented silicon steel sheet (GOSSS) [3], [4]. On the one hand, the vibration of the ASR core will produce noise pollution in the surrounding environment, affecting the health of workers and nearby residents. On the other hand, vibration and noise can cause internal faults in the ASR (e.g., loose iron core, deformed winding, and insulation deterioration) [5], [6], [7]. By investigating the vibration characteristics of the ASR core, this study establishes a theoretical foundation for optimizing the structural design fault detection of the ASR. Meanwhile, the study is the basic to evaluate the long-term effects of these vibrations on the ASR's performance and reliability over time.

At present, there are few studies on the vibration and noise of the ASR core, most of which focus on the vibration of motors which can guide the study of the ASR [8], [9], [10]. Due to the gap between stator and rotor, the Maxwell stress as the main source of motor vibration has received more attention. However, the magnetostrictive stress should not be ignored in the research of the ASR core. In addition, the nonoriented silicon steel sheet (NOSSS) is used in motor cores, while the GOSSS with intense anisotropic characteristics is used in reactors [11]. The most significant difference between them is the orientation distribution function of the grains in the sheet plane. The grains in NOSSS are disorderly distributed causing greater magnetostriction and vibration than that of GOSSS when the GOSSS has more intense anisotropy in the magnetic field and mechanical field [12], [13], [14]. Therefore, the anisotropic magnetostriction of the GOSSS needs to be measured accurately to calculate the vibration and noise of the ASR core. Finite element analysis (FEA) is an effective way to establish a connection between the magnetic properties of the GOSSS and the vibration characteristics of the ASR core. To save calculation time under the premise of ensuring the accuracy of calculation, the homogenization method of the type-wound core in the magnetic field has been proposed and verified based on the equivalent of core loss [15], [16]. The method makes it possible to simplify the lamination model to a solid model in the calculation. Meanwhile, the components of silicon steel sheets with insulation paste

Received 16 March 2025; revised 26 June 2025; accepted 3 August 2025. Date of publication 25 August 2025; date of current version 5 September 2025. This work was supported in part by the National Natural Science Foundation of China under Grant 52277008, in part by the Natural Sciences Foundation of Hebei Province under Grant E2023202050, in part by the Funds for Creative Research Groups of Hebei Province under Grant E2024202298, and in part by the Innovation Ability Training Funding Project for Doctoral Students in Hebei Province under Grant CXZZBS2025050. The Associate Editor coordinating the review process was Dr. Shiraz Sohail. *(Corresponding author: Changgeng Zhang.)*

Tao Chen, Qingxin Yang, Changgeng Zhang, Yongjian Li, and Shuaichao Yue are with the State Key Laboratory of Intelligent Power Distribution Equipment and System, Hebei University of Technology, Tianjin 300130, China (e-mail: 202311401017@stu.hebut.edu.cn; qxyang@tjpu.edu.cn; changgeng.zhang@hebut.edu.cn; liyongjian@hebut.edu.cn; yues22@hebut.edu.cn).

Yu Dou is with Zhejiang University–University of Illinois at Urbana–Champaign Institute, Zhejiang University, Haining 314400, China (e-mail: yudou@intl.zju.edu.cn).

Digital Object Identifier 10.1109/TIM.2025.3602530

1557-9662 © 2025 IEEE. All rights reserved, including rights for text and data mining, and training of artificial intelligence and similar technologies. Personal use is permitted, but republication/redistribution requires IEEE permission.
See https://www.ieee.org/publications/rights/index.html for more information.

Authorized licensed use limited to: Hebei University of Technology. Downloaded on September 12,2025 at 02:31:59 UTC from IEEE Xplore. Restrictions apply.

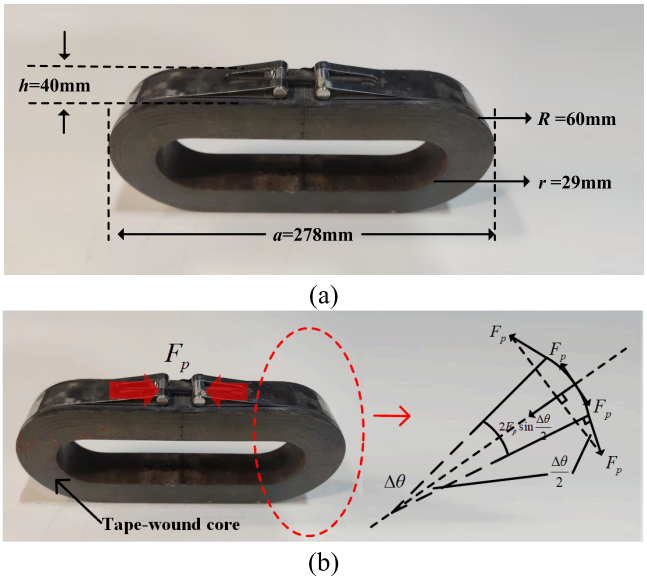


Fig. 1. Diagram of the ASR core. (a) Dimensions of the ASR core. (b) Bolt pre-tightening force acts on the ASR core.

vary greatly in spatial scale and mechanical properties. The homogenization method applied in the vibration simulation of the ASR core needs to consider the equivalent mechanical properties of silicon steel sheets and insulation paste.

In this article, the vibration mechanism of the core is clarified by analyzing the vibration source of the ASR core. Based on the theoretical analysis, the vibration characteristics of the core are studied from simulation and experimental measurements. First, the homogenization method is proposed and the anisotropic magnetic and mechanical material properties of the GOSSS are measured experimentally. The anisotropic material properties are used in the magnetic–mechanical coupling simulation by the finite element method to obtain the distribution of the magnetic flux density and stress. Then, the vibration measuring platform is built and the vibration characteristics of the core are analyzed in both the time domain and frequency domain. The uncertainty of the measurement is analyzed and measures to improve the stability of the measurement results are proposed. Finally, the error between the simulation and experimental results is calculated by comparing the vibration velocity of the core.

II. Analysis of Vibration Theory

The ASR core is wound by the tape of ultrathin GOSSS. In order to control the inductance of the ASR core and facilitate installation, the tape-wound core is divided into two U-shaped cores and then bound together by the steel strap and bolt. The inductance of the core can be changed by adjusting the width of the air gap between the two U-shaped cores. During operation, the vibration and acoustic noise are generated under the action of the pre-tightening force, magnetostrictive stress, and Maxwell stress analyzed as follows.

A. Pre-Tightening Force

The core is subjected to the pre-tightening force because of the binding of the steel strap and bolt as shown in Fig. 1(a). The effect of the force acting on the round corner is the most obvious and the unit angle is extracted as shown in Fig. 1(b), where F_p represents the pre-tightening force from the steel strap and bolt.

The surface force density σ_P is brought by the pre-tightening force on the contact surface between the core and the steel strap, as shown in the following equation:

$$\frac{\partial \sigma_P}{\partial r} = \frac{2F_p \sin(\Delta\theta/2)}{hR\Delta\theta} \tag{1}$$

where h is the thickness of the core and R is the outer radius of the corner part of the core. Equation (1) is reduced to (2) as $\Delta\theta$ approaches zero

$$\frac{\partial \sigma_P}{\partial r} = \lim_{\Delta\theta\to 0} \frac{2F_p \sin(\Delta\theta/2)}{hR\Delta\theta} = \frac{F_p}{hR}. \tag{2}$$

B. Magnetostrictive Stress

The magnetostrictive coefficient describes the magnitude of magnetostrictive strain, which is expressed as follows:

$$\lambda = \Delta L/L \tag{3}$$

where ΔL denotes the displacement of the GOSSS along the magnetic field direction and L denotes the total length of the GOSSS in the displacement direction. The function is used to represent the variation of magnetostrictive strain $\boldsymbol{\varepsilon}_{\mathrm{MS}}$ with magnetic flux density in this article based on the experimental measurements, as shown in the following equation:

$$\varepsilon_{\mathrm{MS}} = \frac{3}{2}\begin{pmatrix} \lambda_{100}\left(\gamma_1^2 - \frac{1}{3}\right) & \lambda_{111}\gamma_1\gamma_2 & \lambda_{111}\gamma_1\gamma_3 \\ \lambda_{111}\gamma_1\gamma_2 & \lambda_{100}\left(\gamma_2^2 - \frac{1}{3}\right) & \lambda_{111}\gamma_2\gamma_3 \\ \lambda_{111}\gamma_1\gamma_3 & \lambda_{111}\gamma_2\gamma_3 & \lambda_{100}\left(\gamma_3^2 - \frac{1}{3}\right) \end{pmatrix} \tag{4}$$

where γ_k^α is the direction cosine of magnetization vector and λ_{100} and λ_{111} are two so-called cubic magnetostriction constants measured in the experiments. According to generalized Hooke's law, the magnetostrictive stress $\boldsymbol{\sigma}_{\mathrm{MS}}$ is governed by the following equation:

$$\boldsymbol{\sigma}_{\mathrm{MS}} = \left[S_{ij}\right]^{-1} \varepsilon_{\mathrm{MS}} \tag{5}$$

where $[S_{ij}]$ denotes the flexibility matrix, as shown in the following equation:

$$\left[S_{ij}\right] = \begin{bmatrix} 1/E_1 & -\nu_{21}/E_2 & -\nu_{31}/E_3 & 0 & 0 & 0 \\ -\nu_{12}/E_1 & 1/E_2 & -\nu_{32}/E_3 & 0 & 0 & 0 \\ -\nu_{13}/E_1 & -\nu_{23}/E_2 & 1/E_3 & 0 & 0 & 0 \\ 0 & 0 & 0 & 1/G_{23} & 0 & 0 \\ 0 & 0 & 0 & 0 & 1/G_{31} & 0 \\ 0 & 0 & 0 & 0 & 0 & 1/G_{12} \end{bmatrix} \tag{6}$$

where $\mathbf{E}_i$ denotes Young's modulus, $\boldsymbol{\nu}_{ij}$ denotes Poisson's ratio, $\mathbf{G}_{ij}$ denotes shear modulus, and i and j denote coordinates of the elements of the matrix $(i, j = 1, 2, 3)$.

C. Maxwell Stress Tensor

The Maxwell stress tensor $\boldsymbol{\sigma}_M$ is calculated from the magnetic flux density $\mathbf{B}$ and magnetic field intensity $\mathbf{H}$, as shown in the following equation:

$$\boldsymbol{\sigma}_M = \mathbf{B} \otimes \mathbf{H} - (1/2)\,\mu_0\,(\mathbf{H} \cdot \mathbf{H})\,\mathbf{I} \tag{7}$$

Authorized licensed use limited to: Hebei University of Technology. Downloaded on September 12,2025 at 02:31:59 UTC from IEEE Xplore. Restrictions apply.

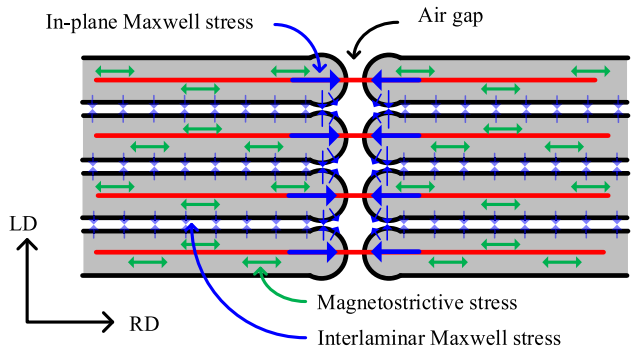


Fig. 2. Stress distribution of the ASR core with air gap.

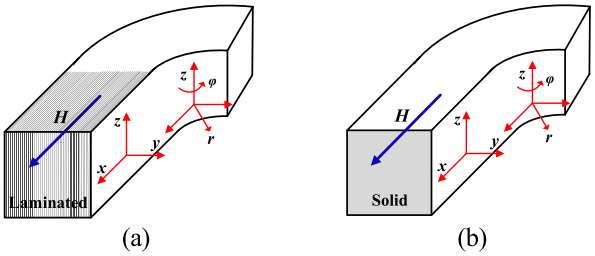


Fig. 3. Homogenized geometric model of the ASR core. (a) Laminated core. (b) Homogenized core.

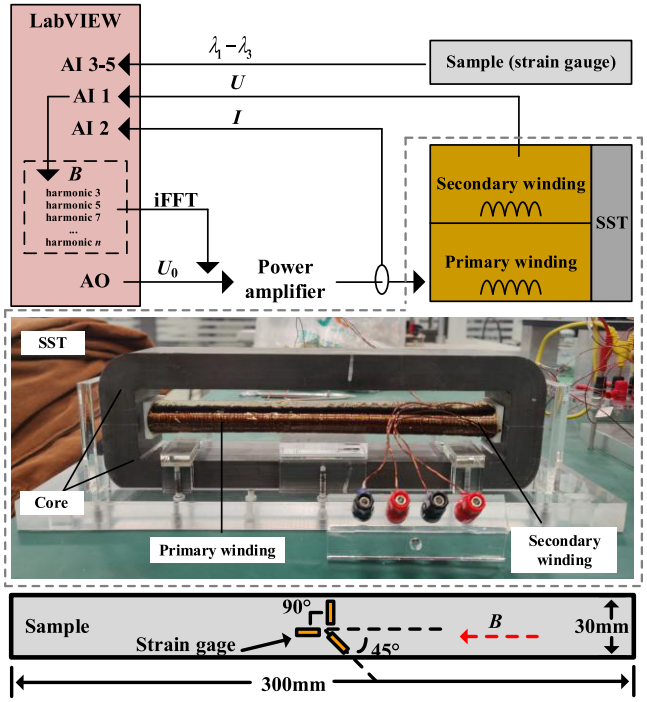


Fig. 4. Magnetic and magnetostrictive properties measuring system and samples.

where **I** is a unit tensor. The magnetic flux density is not entirely perpendicular to the cutting surface through the air gap during the operation, resulting in multiple nonzero components of the Maxwell stress tensor. At the same time, there is a weak magnetic flux between layers of silicon steel sheet inside the core, which leads to vibration in the laminated direction of the core. The stress distribution of the ASR core is shown in Fig. 2, where LD denotes the "laminated direction" and RD denotes the "rolling direction."

The core is affected by three kinds of stress, and the total stress σ_T is shown in the following equation:

$$\boldsymbol{\sigma}_T = \boldsymbol{\sigma}_P + \boldsymbol{\sigma}_{\mathrm{MS}} + \boldsymbol{\sigma}_M. \tag{8}$$

III. Finite Element Simulation

The finite element model of the ASR core is established based on the magnetic and mechanical anisotropic properties of ultrathin GOSSSs. The magnetic–mechanical coupling simulation is conducted to obtain the magnetic and vibration characteristics of the ASR core.

A. Anisotropic Homogenized Material Model

To save computing resources and reduce computing difficulty, the homogenization method is applied in the simulation of the ASR core based on the magnetic and mechanical anisotropic properties of ultrathin GOSSS, as shown in Fig. 3. Fig. 3(a) shows the partial geometric model of the ASR core laminated by the GOSSS and Fig. 3(b) shows the homogenized geometric model of the core by using the homogenization method. The circumferential, radial, and axial directions of the core correspond to the rolling, laminated, and transverse direction of the GOSSS, respectively. The local coordinate system is defined at different regions of the core.

The homogenization method not only differs from the traditional model in the geometric model but also has some definitions in the parameter definition of the core material. In the homogenization method, the permeability $\boldsymbol{\mu}$ and electric conductivity $\boldsymbol{\rho}$ are calculated according to [15] and [16]. The equivalent density ρ_e, Young's modulus **E**, Poisson's ratio **v**, and Shear modulus **G** are derived from (9) to (12), as shown at the bottom of the next page, based on lamination theory [17] where ρ_s and ρ_{ins} are the density of the GOSSS and insulation paste, respectively; F_l is the laminated coefficient of the core; $E_{s(r)}, E_{s(t)}$, and $E_{s(l)}$ are Young's modulus in the rolling, transverse, and laminated directions of the GOSSS, respectively; $\nu_{s(rt)}, \nu_{s(tr)}, \nu_{s(rl)}, \nu_{s(lr)}, \nu_{s(tl)}$, and $\nu_{s(lt)}$ are the anisotropic Poisson's ratio of the GOSSS; E_{ins} and ν_{ins} are Young's modulus and Poisson's ratio of the insulation paste, respectively; and $G_{s(rl)}, G_{s(tl)}$, and $G_{s(rt)}$ are Shear modulus of the GOSSS, which are calculated from (13) to (15). G_{ins} is the Shear modulus of the insulation paste

$$G_{s(rl)} = \frac{E_{s(l)}E_{s(r)}}{E_{s(l)}(1+\nu_{rl}) + E_{s(r)}(1+\nu_{lr})} \tag{13}$$

$$G_{s(tl)} = \frac{E_{s(l)}E_{s(t)}}{E_{s(l)}(1+\nu_{tl}) + E_{s(t)}(1+\nu_{lt})} \tag{14}$$

$$G_{s(rt)} = \frac{E_{s(t)}E_{s(r)}}{E_{s(t)}(1+\nu_{rt}) + E_{s(r)}(1+\nu_{tr})}. \tag{15}$$

The magnetic and magnetostrictive properties of the GOSSS in the rolling direction and transverse direction are obtained by

Authorized licensed use limited to: Hebei University of Technology. Downloaded on September 12,2025 at 02:31:59 UTC from IEEE Xplore. Restrictions apply.

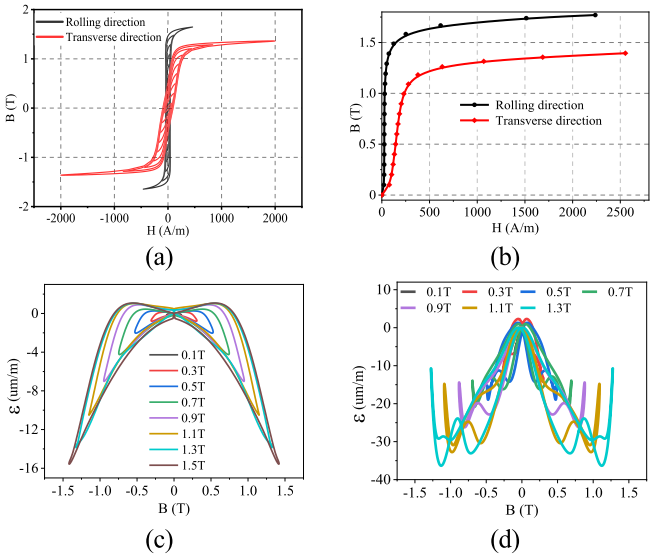


Fig. 5. Measurement results of magnetic and magnetostrictive properties. (a) Hysteresis loops. (b) No-hysteresis magnetization curves. (c) Butterfly curve in the rolling direction. (d) Butterfly curve in the transverse direction.

experimental measurements according to IEC standard 62581 [18]. The measuring system and samples are shown in Fig. 4. The primary current and secondary voltage are measured to calculate the magnetic field intensity and the magnetic flux density. The feedback control algorithm is used to ensure that the waveform of the magnetic flux density is sinusoidal [19]. The measurement results are shown in Fig. 5. As shown in Fig. 5(a), the *B–H* curve in the rolling direction of the GOSSS is more inclined compared with the curve in the transverse direction, which indicates that the GOSSS is more easily magnetized in the rolling direction, and the core loss is lower

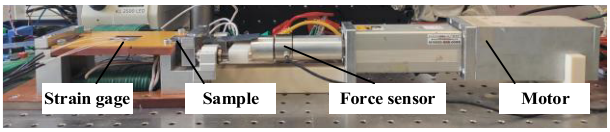


Fig. 6. Device for measuring mechanical properties of the GOSSS.

in the rolling direction. What is more, the GOSSS has lower coercivity and higher permeability in the rolling direction. It can also be seen from Fig. 5(b) that the amplitude of magnetic field intensity required to achieve the same amplitude of magnetic flux density is lower in the rolling direction. For example, when the magnetic field is along the rolling direction, the magnetic flux density of the GOSSS with 1.0 T needs the magnetic field with 29.7 A/m, but 230.7 A/m is required in the transverse direction. In conclusion, the GOSSS has intense magnetic anisotropy and has more dominant magnetic properties in the rolling direction.

The resistance strain gauge is pasted on the surface of the GOSSS in the 0°, 45°, and 90° direction to measure vectorial magnetostriction as shown in Fig. 5(c) and (d). The GOSSS exhibits negative magnetostriction in both rolling direction and transverse direction. With the increase of the amplitude of magnetic flux density, the peak-to-peak value of the magnetostriction increases gradually, and the transverse magnetostriction is higher than the rolling direction at all levels of the magnetic flux density. The results show that the magnetostriction of the GOSSS also has intense anisotropy.

The mechanical anisotropy properties of the GOSSS are also measured according to the ISO standard [20] and ASTM standard [21]. The measuring device and results are shown in Figs. 6 and 7, respectively. The tensile stress is applied to the GOSSS by a motor, which is monitored by the force

$$\rho_e = F_l \rho_s + (1 - F_l)\,\rho_{\text{ins}} \tag{9}$$

$$E = \begin{bmatrix} E_{s(r)}F_l + E_{\text{ins}}(1-F_l) & 0 & 0 \\ 0 & \dfrac{1}{\dfrac{F_l}{E_{s(t)}} + \dfrac{(1-F_l)}{E_{\text{ins}}}} & 0 \\ 0 & 0 & E_{s(t)}F_l + E_{\text{ins}}(1-F_l) \end{bmatrix} \tag{10}$$

$$\nu = \begin{bmatrix} 1 & \dfrac{1}{\dfrac{F_l}{\nu_{s(rl)}} + \dfrac{(1-F_l)}{\nu_{\text{ins}}}} & \nu_{s(rt)}F_l + \nu_{\text{ins}}(1-F_l) \\ \dfrac{1}{\dfrac{F_l}{\nu_{s(lr)}} + \dfrac{(1-F_l)}{\nu_{\text{ins}}}} & 1 & \dfrac{1}{\dfrac{F_l}{\nu_{s(lt)}} + \dfrac{(1-F_l)}{\nu_{\text{ins}}}} \\ \nu_{s(tr)}F_l + \nu_{\text{ins}}(1-F_l) & \dfrac{1}{\dfrac{F_l}{\nu_{s(tl)}} + \dfrac{(1-F_l)}{\nu_{\text{ins}}}} & 1 \end{bmatrix} \tag{11}$$

$$G = \begin{bmatrix} 0 & \dfrac{G_{s(rl)}G_{\text{ins}}}{G_{s(rl)}F_l + G_{\text{ins}}(1-F_l)} & G_{s(rt)}F_l + G_{\text{ins}}(1-F_l) \\ \dfrac{G_{s(rl)}G_{\text{ins}}}{G_{s(rl)}F_l + G_{\text{ins}}(1-F_l)} & 0 & \dfrac{G_{s(tl)}G_{\text{ins}}}{G_{s(tl)}F_l + G_{\text{ins}}(1-F_l)} \\ G_{s(rt)}F_l + G_{\text{ins}}(1-F_l) & \dfrac{G_{s(tl)}G_{\text{ins}}}{G_{s(tl)}F_l + G_{\text{ins}}(1-F_l)} & 0 \end{bmatrix} \tag{12}$$

Authorized licensed use limited to: Hebei University of Technology. Downloaded on September 12,2025 at 02:31:59 UTC from IEEE Xplore. Restrictions apply.

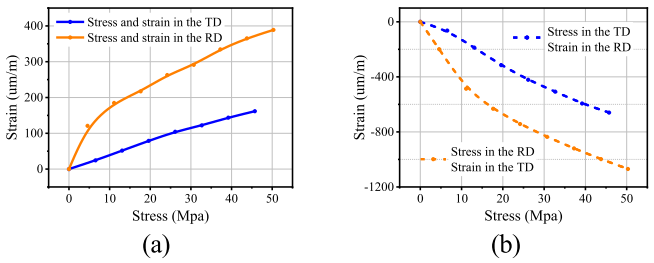


Fig. 7. Stress–strain curves of the GOSSS. (a) Principal stress–strain curves. (b) Shear stress–strain curves.

TABLE I
MAGNETIC AND MECHANICAL PROPERTIES

F_l	ρ_c (S/m)	E_{ins} (GPa)	ν_{ins}	ρ_s (g/cm^3)	ρ_{ins} (g/cm^3)
0.98	1.98e+6	50	0.25	7.65	1.0

$\boldsymbol{\mu}_s$	$\mathbf{E}_s$ (GPa)	$\boldsymbol{\nu}_s$
$\begin{bmatrix} \mu_r(H) & 0 \\ 0 & \mu_t(H) \end{bmatrix}$	$\begin{bmatrix} 112 & 0 & 0 \\ 0 & 263 & 0 \\ 0 & 0 & 263 \end{bmatrix}$	$\begin{bmatrix} 1 & 0.28 & 0.28 \\ 0.29 & 1 & 0.29 \\ 0.29 & 0.28 & 1 \end{bmatrix}$

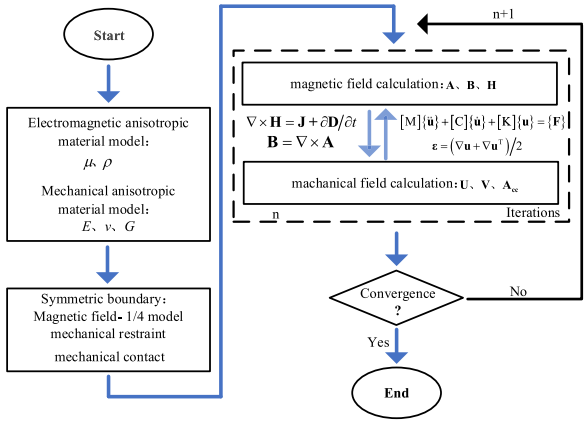


Fig. 8. Flowchart of the simulation.

sensor. The resistance strain gauge is used to measure the strain generated by the GOSSS. The strain changes with stress linearly in the elastic deformation stage, as shown in Fig. 7.

In summary, the mechanical properties of the GOSSS and insulating paste measured by experiments are shown in Table I.

B. Simulation Principle

Fig. 8 shows the flowchart of the simulation to obtain the distribution of the magnetic flux density and stress of the core. The contact between the steel strap and the core is modeled by the penalty function method [22]. The magnetic and mechanical fields are solved iteratively using the Newton–Raphson method.

C. Results and Analysis

The effect of magnetomotive force (MMF) and air-gap width on the distribution of the magnetic flux density of the core is studied, as shown in Fig. 9. For the runway-shaped core, the magnetoresistance in the inner part is lower than that in the outer part, causing a higher magnetic flux density in the

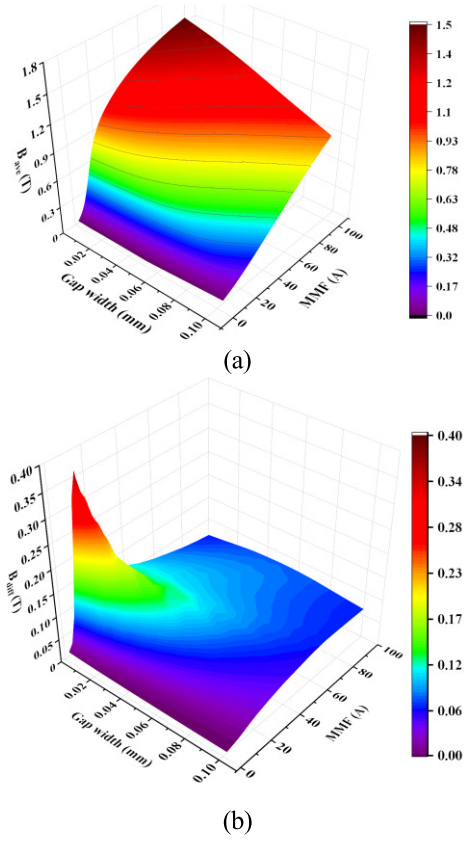


Fig. 9. Distribution of the magnetic flux density of the core. (a) Average magnetic flux density in the core section. (b) Difference between the inside and outside the core.

inner part [23]. With the increase of the MMF, the difference between the magnetic flux density inside and outside the core (B_{diff}) gradually increases and reaches a peak value of 0.39 T when the MMF equals 30 A, and the mean magnetic flux density (B_{ave}) of the core section is 0.56 T at the same time. When the MMF increases further, B_{diff} decreases gradually and approaches 0 T. The difference in the distribution of the magnetic flux density is reduced because of the air gap. When the width of the air gap increases, B_{ave} and B_{diff} decreases. The peak value of B_{diff} is greatly reduced if the MMF is increased.

Fig. 10(a) shows the simulated curve of the winding current, magnetic flux density, and vibration displacement. The magnetic flux density is the average magnetic flux density of the core section, the vibration displacement u_1 is located near the air gap, and the vibration displacement u_2 is located near the corner. It can be seen from the results that the vibration frequency of the core is twice the excitation frequency. The vibration modes of the core are studied in detail at the moments of A–E, as shown in Fig. 10(b).

In state A, the core is in the initial mode and subjected to the pre-tightening force (1000 N is defined in the simulation) generated by the steel strap and bolt. From state A to state C, the winding current and magnetic flux density of the core gradually increase. Meanwhile, the circumferential deformation near the air gap increases first and decreases with time, while the radial deformation at the corner always increases. From state C to state E, the winding current and magnetic flux density of the core gradually decrease with the increase

Authorized licensed use limited to: Hebei University of Technology. Downloaded on September 12,2025 at 02:31:59 UTC from IEEE Xplore. Restrictions apply.

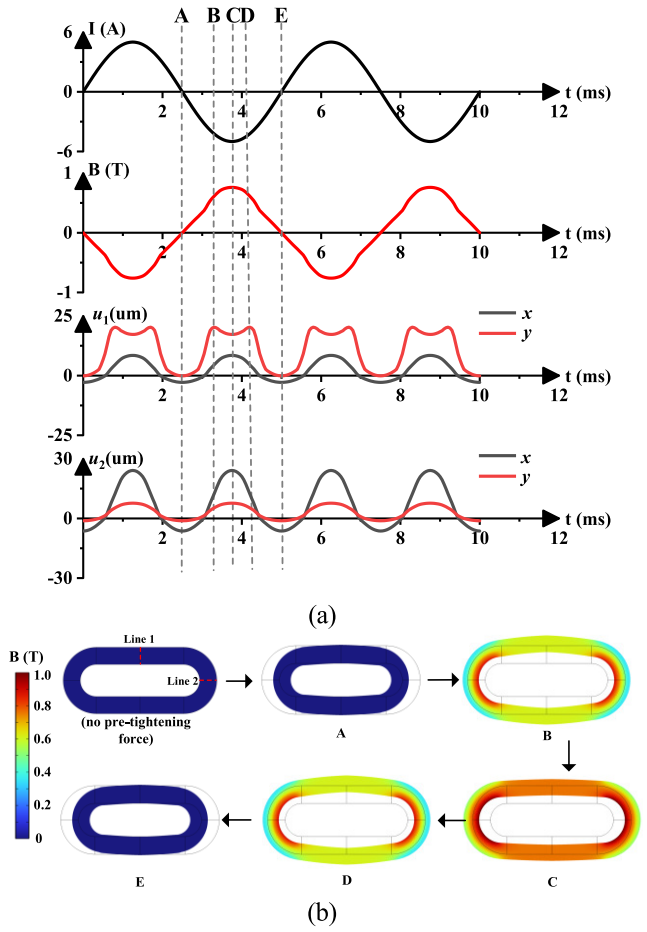


Fig. 10. (a) Variable curves in the time domain and (b) vibration modes of the ASR core.

of time. The deformation trend of the core inversely changes with the first half cycle.

The magnetic flux density and stress in the core along the air-gap sampling line [Line 1 shown in Fig. 10(b)] change periodically, as shown in Fig. 11(a) and (b). The magnetic flux density and stress in the core along the corner sampling line [Line 2 shown in Fig. 10(b)] are shown in Fig. 11(c) and (d). Compared with (a) and (c), the magnetic flux density at line 1 is more uniform because of the air gap and the magnetic flux density on the inside of the core at line 2 is greater than that on the outside because of the magnetoresistance. The core mainly exhibits expansion mode during vibration, as shown in Fig. 10(b). Therefore, the stress on the inside of the core is always higher than that on the outside, as shown in Fig. 11(b) and (d). The maximum stress near the core corner is higher than that near the air gap.

IV. Experiment and Results

A vibration measuring platform is built in the anechoic chamber based on the MB dynamic M50 vibrator, the PSV QTec HV scanning vibrometer, and so on, as shown in Fig. 12. The magnetic and vibration characteristics of the core are measured under varying frequencies and magnetic flux densities. The uncertainty of the measurement is analyzed, and measures to ensure the stability of the measurement results are proposed. The simulation results are verified by the experimental results.

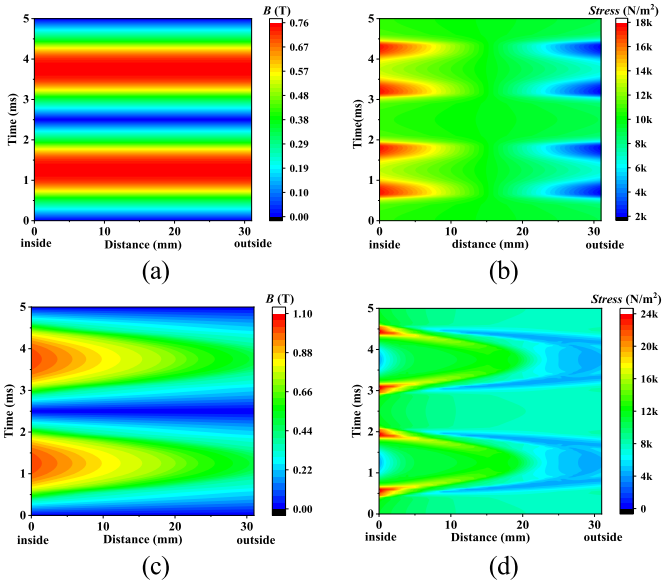


Fig. 11. (a) and (c) Magnetic flux density. (b) and (d) Stress along the air-gap sampling line and the corner sampling line, respectively.

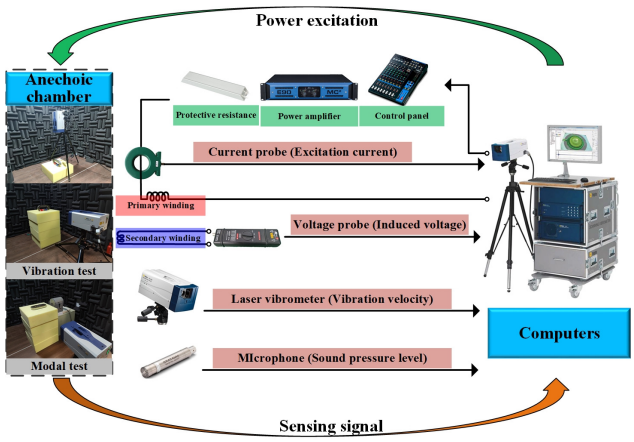


Fig. 12. Vibration measuring platform of the ASR core.

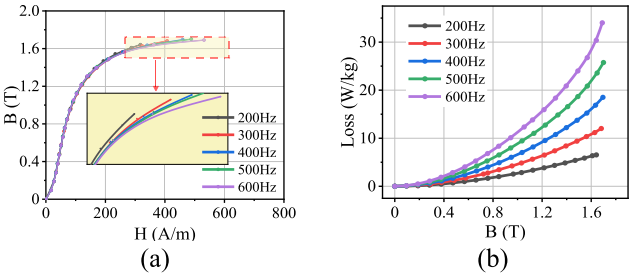


Fig. 13. Normal (a) magnetization curves and (b) loss curves of the ASR core.

A. Magnetic Property Measurement of ASR Core

The magnetic permeability and loss properties of the ASR core under sine excitation are measured and analyzed, as shown in Fig. 13.

When the magnetic field intensity reaches 100 A/m, the magnetization of the core enters the nonlinear region, and the magnetization curve reaches the knee point. When the magnetic field intensity is about 500 A/m, the magnetization of

Authorized licensed use limited to: Hebei University of Technology. Downloaded on September 12,2025 at 02:31:59 UTC from IEEE Xplore. Restrictions apply.

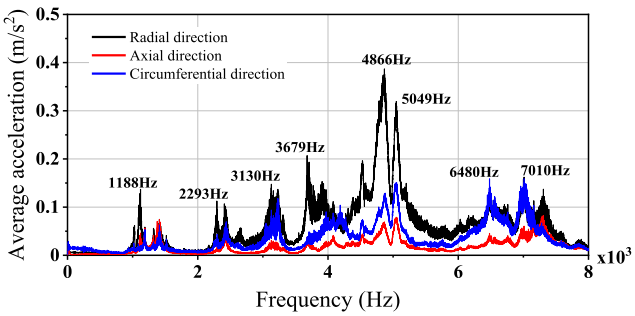


Fig. 14. Frequency response curve of the core vibration.

the core is close to saturation. The loss curve under sinusoidal magnetization of 200–600 Hz is shown in Fig. 13(b). The core loss gradually increases with the increase of magnetic flux density and reaches 6.36 W/kg at 200 Hz and 1.6 T. With the frequency increase, the increasing rate of the core loss is larger.

B. Mode Measurement of ASR Core

The natural frequencies as an inherent property of the core affect the vibration mode. When the vibration frequency of the core coincides with the natural frequencies, mechanical resonance will occur and the vibration intensity of the core will be significantly enhanced. In this article, the natural frequencies of the core are measured by experiment based on the measuring platform, as shown in Fig. 12. The core is placed on a highly elastic spongy cushion to assume that the bottom of the core is a free boundary. In the process of measurement, the exciting force of the sweeping frequency is applied to the core by the MB dynamic M50 vibrator, and the vibration velocity of the core is collected by the PSV QTec HV scanning vibrometer.

Fig. 14 shows the frequency response curve of the core vibration during the mode measurement. The horizontal axis represents the sweep frequency range of the vibration of the core, and the vertical axis represents the amplitude of the vibration. The three curves with different colors represent vibrations along the core in radial, axial, and circumferential directions. The "peak" on the curve means that the core vibrates more intense at this frequency and the natural frequency of the core is located at here. As can be seen from Fig. 14, the vibration resonated near the frequencies of 1188 Hz and so on.

C. Measurements of the Core Vibration

The array of measurement points is arranged on the outer surface of the core, as shown in Fig. 15. The secondary voltage of the core is used to synchronize vibration velocity and magnetic flux density in every measurement at each point.

The equivalent vibration velocity measured on the surface of the core at 200 Hz is shown in Fig. 16 calculated by the following equation:

$$V_{\text{rms}} = \sqrt{\frac{1}{n}\sum_{i=1}^{n}\tilde{v}_i^2} \tag{16}$$

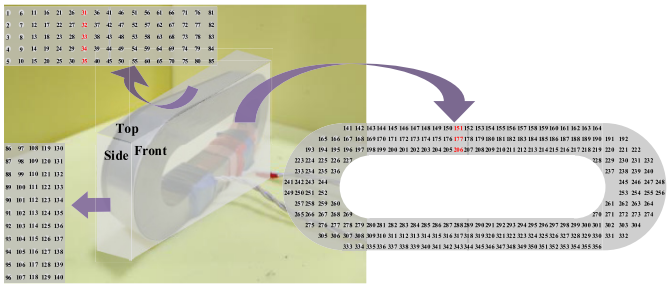


Fig. 15. Array diagram of measurement points.

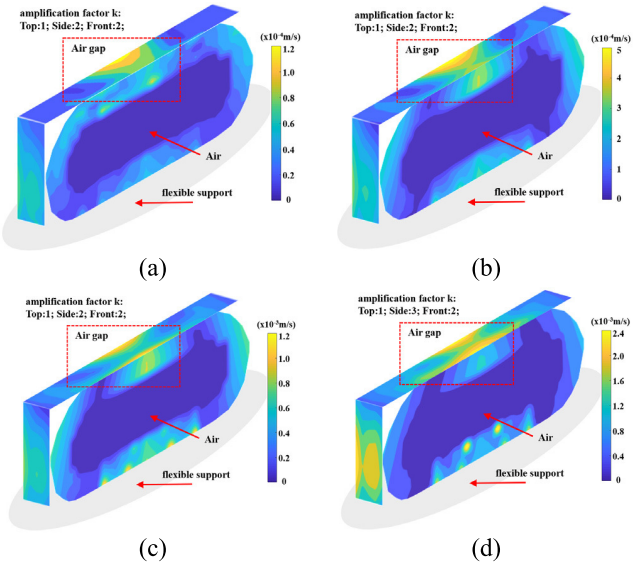


Fig. 16. Vibration velocity cloud image of the core at 200 Hz with (a) 0.3, (b) 0.7, (c) 1.1, and (d) 1.5 T.

where n is the number of sampling points in a vibration period and $\tilde{v}_i$ represents the instantaneous vibration velocity.

The radial vibration of the core is the most intense and the points with the highest vibration intensity are located near the air gap which reaches 2.4 mm/s at 1.5 T. Since the steel strap is not stuck to the core by epoxy glue, the vibration velocity of the steel strap is slightly lower than that of the core surface, as shown in the top and side faces of the core in Fig. 16.

Points 31–35, 151, 177, and 206 marked in Fig. 15 are selected as the measurement points to analyze the vibration velocities. The instantaneous vibration velocity obtained at 200 Hz is shown in Fig. 17. With the continuous increase of the magnetic flux density of the core, the amplitude of vibration velocity keeps increasing and the waveforms of vibration velocity remain sinusoidal. When the magnetic flux density of the core enters the nonlinear stage, the harmonic contents significantly increase. Although the power frequency is far from the natural frequency of the core, the twice frequency or higher harmonics frequency in the component of the magnetic flux density may be close to the natural frequency. Mechanical resonance occurs, and the vibration of the core is enhanced. The harmonic analysis of vibration velocity is performed at point 31 and the frequency spectrum diagram is shown in Fig. 18.

The vibration frequency of the core is mainly twice the power frequency at low magnetic flux density. Then, the

Authorized licensed use limited to: Hebei University of Technology. Downloaded on September 12,2025 at 02:31:59 UTC from IEEE Xplore. Restrictions apply.

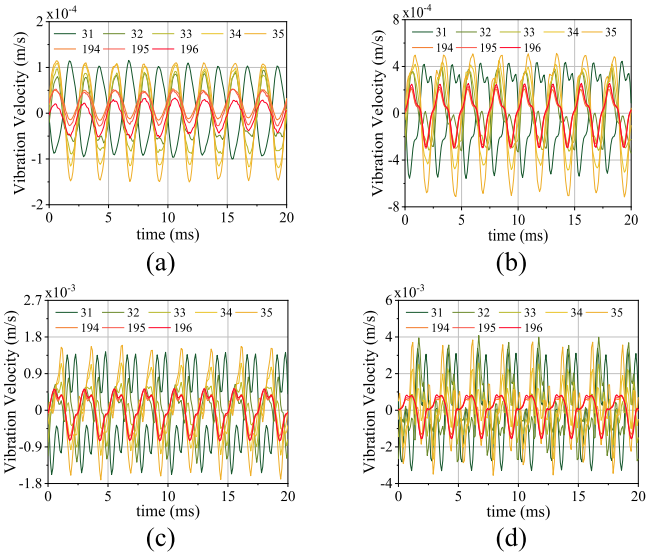


Fig. 17. Vibration velocity waveforms of the measurement points at 200 Hz with (a) 0.3, (b) 0.7, (c) 1.1, and (d) 1.5 T.

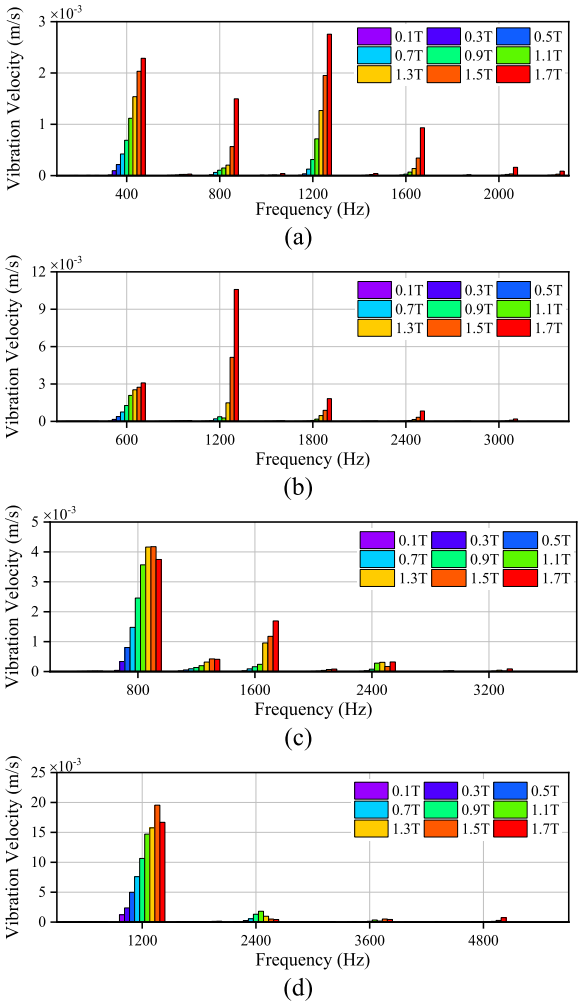


Fig. 18. Vibration velocity spectrum diagram at the measurement point 31 and (a) 200, (b) 300, (c) 400, and (d) 600 Hz.

nonlinear hysteresis effect gradually plays a role at high magnetic flux density. Harmonics begin to appear in the magnetic flux density which leads to a greater vibration at

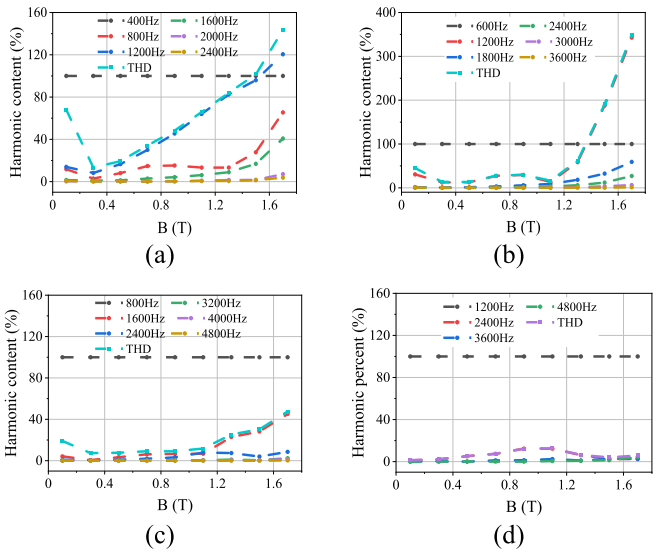


Fig. 19. THD of the vibration velocity at (a) 200, (b) 300, (c) 400, and (d) 600 Hz.

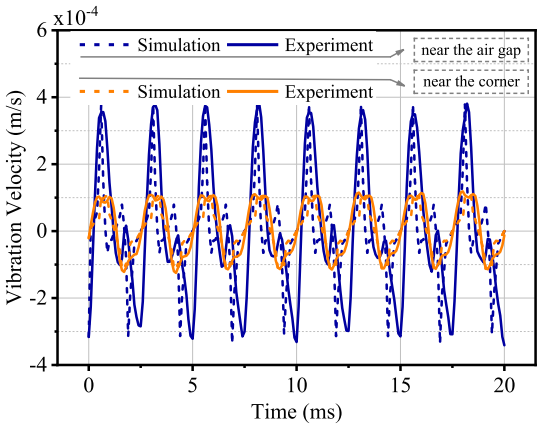


Fig. 20. Curves of vibration velocity in the experiment and simulation.

twice the power frequency. At the same time, the vibration will be enhanced. The core vibrates mainly at 400 Hz when the excitation frequency is 200 Hz and the magnetic flux density is less than 1.5 T as shown in Fig. 18. However, the third harmonic content of the magnetic flux density of the core increases at 1.7 T, resulting in the largest vibration component at twice the frequency of the third harmonic which is 1200 Hz. According to the vibration velocity spectrum diagram of the core vibration at the power frequencies of 200, 300, 400, and 600 Hz, it can be judged that the resonance occurs near 1200 Hz, which is consistent with the mode analysis as shown in Fig. 14. The total harmonic distortion (THD) of the vibration velocity waveform shown in Fig. 19 is calculated as follows:

$$\mathrm{THD} = \sqrt{\sum_{h=1}^{m} \left(V_h^2 - V_1^2\right) \Big/ V_1^2} \tag{17}$$

where V_1 is the vibration under fundamental frequency and V_h is the vibration under the hth harmonic frequency.

Under the high magnetic flux density of the core at 200 and 300 Hz, the primary vibration frequency is no longer twice the

Authorized licensed use limited to: Hebei University of Technology. Downloaded on September 12,2025 at 02:31:59 UTC from IEEE Xplore. Restrictions apply.

excitation frequency. Under the varying magnetic flux density at 400 and 600 Hz, the primary vibration frequency is always twice the excitation frequency. The points near the air gap and the corner are selected to compare the experiment and simulation results under the condition of 0.7 T and 200 Hz, as shown in Fig. 20. The error is 8.76% for the point near the air gap and 8.96% for the point near the corner, which proves the homogenization method presented in this article can effectively calculate the vibration of the ASR core. The error is divided into simulation error and experimental error. Simulation error refers to the deviation during the processing and manufacturing such as uneven thickness of insulating glue, etc. Experimental error is usually caused by the experimental environment and uncontrollable variables. Although attention has been paid during the measurement process, it is still inevitable that there will be a slight impact on the measurement results. Therefore, the uncertainty of the measurement is analyzed and measures to improve the stability of the measurement results are proposed.

D. Analysis of Measurement Uncertainty

During the measurement process of the magnetic properties and the core vibration, the heat within the core from induced eddy current modifies the measurement environment and introduces measurement inaccuracies. Several studies conformed that temperature can affect the magnetic properties of the core [24], [25]. The degree of this influence varies at different frequencies. To systematically quantify thermal effects on measurement outcomes, this research evaluates hysteresis loop characteristics, core losses, and vibrations under varying core temperatures. All thermal effects are strictly limited to core self-heating (eddy current and hysteresis losses), with external thermal management systems deliberately excluded and cooling provided solely by natural convection. Dual constraints of maximum measurement duration (90 min) and peak core temperature (65 °C) are implemented to ensure insulation integrity of core laminations and windings while assessing measurement stability. The temperature rises curve of the core under different frequencies and magnetic flux densities is recorded as shown in Fig. 21(a). Continuous thermal monitoring via infrared imaging within the anechoic chamber facilitated synchronized acquisition of vibration velocities, primary current, and secondary voltage measurements across operational phases. The thermal imaging of the core at different times is shown in Fig. 21(b)–(i).

Due to the slight fluctuations in room temperature (RT) when different measurement groups were carried out, the initial temperatures at 0 min are fluctuates within the range of 5 °C. At the same excitation frequency, the higher magnetic flux density will cause greater eddy current, resulting in the core heating up faster. At identical magnetic flux density levels, the higher the excitation frequency, the more intense the eddy current and the faster the core heats up.

The average vibration velocity derived from 85 measurement points at the top of the core shown in Fig. 15 serves as the representative vibration amplitude. RT, the temperature when the experiment runs for ten minutes (TMs), and the max temperature on each curve (MT) shown in Fig. 21(a) are taken

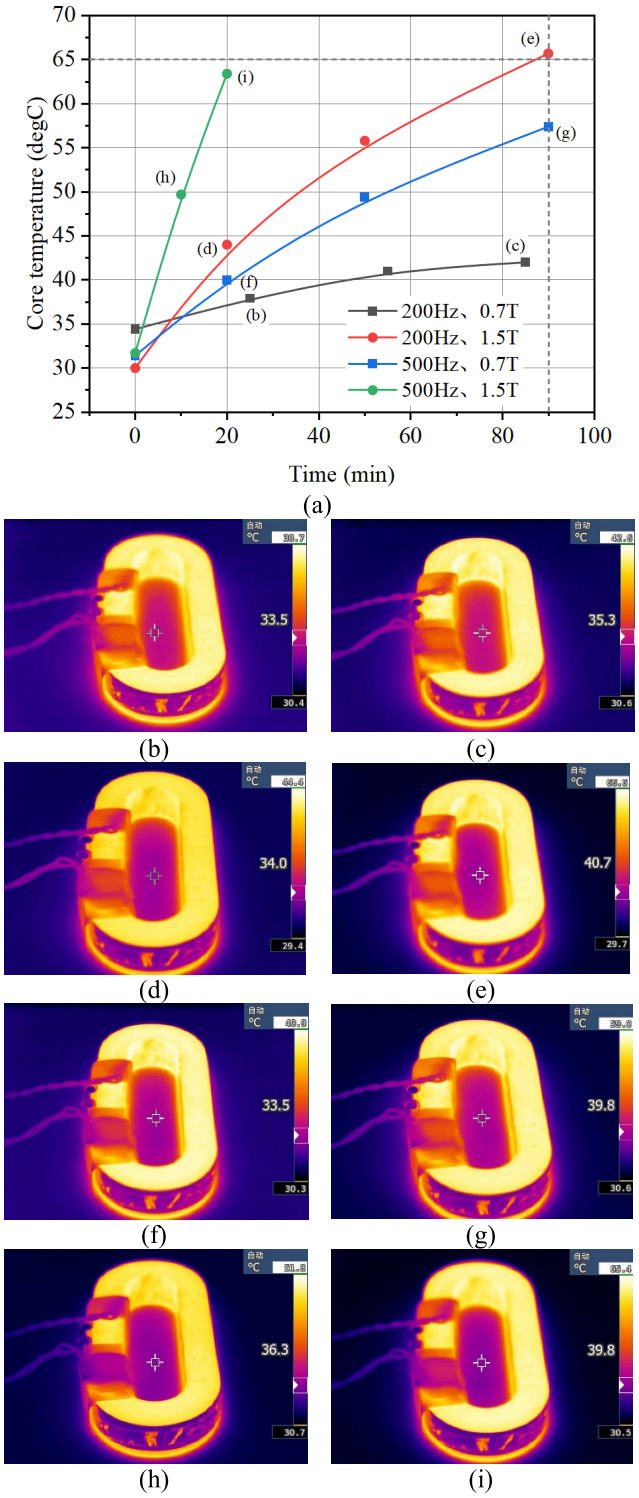


Fig. 21. (a) Temperature rise curve of the core and (b)–(i) thermal imaging at different times.

as different measurement time nodes. The vibration amplitudes, magnetic field intensities, and magnetic flux densities of the core under different experimental groups are obtained as shown in Fig. 22.

The results of the four experimental groups all indicated that the increase in the temperature of the core led to an increase in the vibration velocity with varying amplitudes as shown in Fig. 22(a). When the core is at a low magnetic flux

Authorized licensed use limited to: Hebei University of Technology. Downloaded on September 12,2025 at 02:31:59 UTC from IEEE Xplore. Restrictions apply.

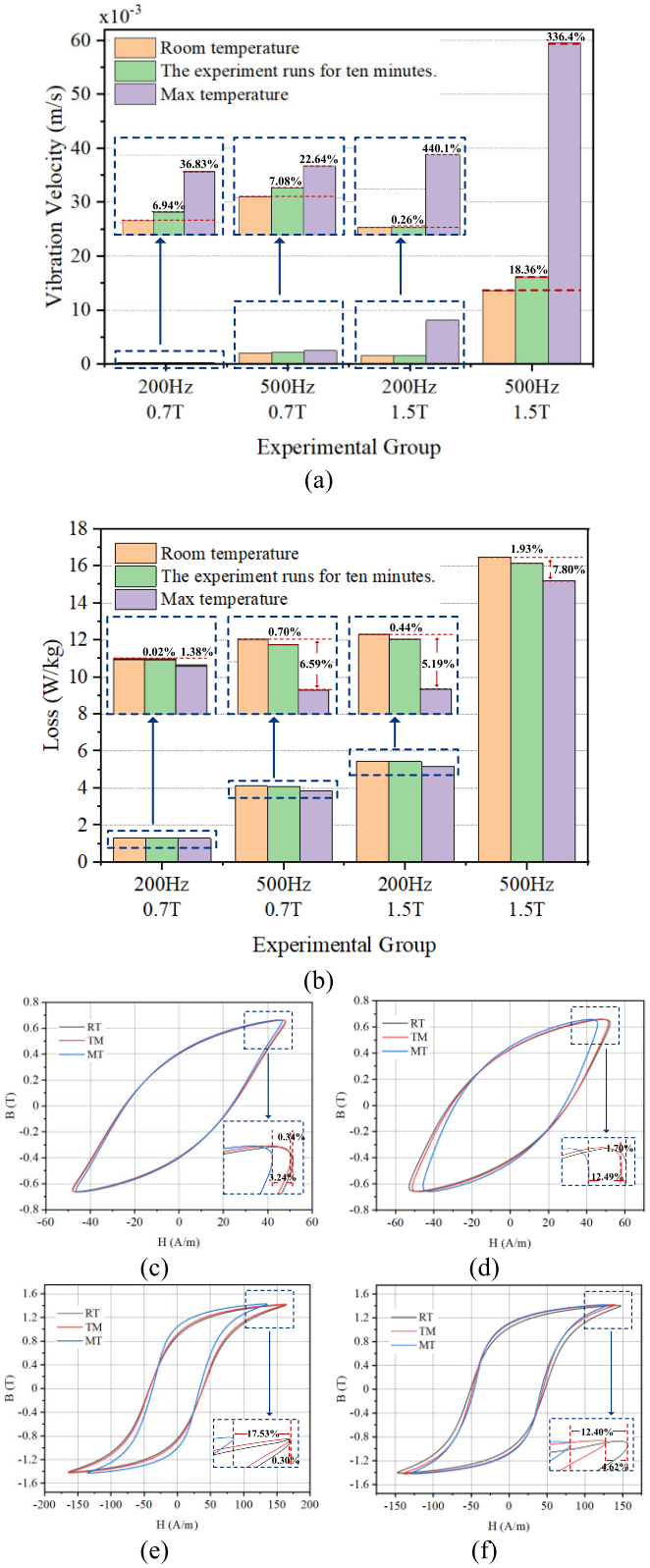


Fig. 22. (a) Vibration amplitudes of the cores in different experimental groups at different measurement time nodes. (b) Core loss in different experimental groups at different measurement time nodes, and the hysteresis loops of the cores at different measurement time nodes under (c) 0.7 T and 200 Hz, (d) 0.7 T and 500 Hz, (e) 1.5 T and 200 Hz, and (f) 1.5 T and 500 Hz.

density (0.7 T), the increase of the vibration velocity with the core temperature is relatively small. The increase at TMs is within 8% and the increase at the max temperature is within 37%. When the core is at a high magnetic flux density (1.5 T), the vibration velocity increases significantly with the core temperature. The increase at TMs reaches 18.36% and the increase at the max temperature reaches 440.1%.

The experimental results demonstrate an inverse correlation between core temperature and power loss. Under 500-Hz excitation at 1.5-T magnetic flux density, the core loss decreases by 1.93% after TMs and 7.8% at the maximum temperature as shown in Fig. 22(b). The magnetic property measurement results of the four experimental groups show that the magnetic field intensity decreases and the magnetic properties of the material change when the core temperature increases as shown in Fig. 22(c)–(f). The maximum change occurred at 200 Hz and 1.5 T. The difference of magnetic field intensities between the max temperature and the RT is 17.53%.

Therefore, in order to enhance the measurement reliability, some methods have been adopted to control the core temperature during the experiment. First, single measurement should be completed within 5 min to avoid a significant increase in the core temperature and the next measurement should start until the core temperature drops to RT. Each experimental group should be conducted at a time when the RT difference is relatively small. Second, since the excitation time at high frequencies is longer than that at low frequencies, a distributed measurement approach is employed by partitioning the flux density range into discrete subintervals, where each measurement session exclusively addressed a designated subinterval. Through the above methods, the experimental error of vibration velocity can be controlled within 5%, the loss error within 1.5%, and the magnetic characteristics of the core are hardly changed. Crucially, active cooling devices such as fans are deliberately avoided to preclude the introduction of extraneous vibrational interference during experimental procedures.

V. Conclusion

In this article, the magnetic and vibration characteristics of the ASR core in the UHVdc converter valve are analyzed from four aspects: theoretical analysis, material properties measurement, simulation, and experimental measurements.

The vibration mechanism of the core is clarified by analyzing the vibration source of the ASR core. During operation, the vibration and acoustic noise are generated under the action of the pre-tightening force, magnetostrictive stress, and Maxwell stress.

The magnetic, magnetostrictive, and mechanical properties of the GOSSS are measured in the experiment, to build the anisotropic material model of the core. The measurement results indicate that the magnetic permeability is higher along the rolling direction than in other directions, while the magnetostriction is higher in the transverse direction than in other directions. The strain is more difficult to occur in the transverse direction than the rolling direction because of the higher Young's modulus. Based on the homogenization method and the finite element method, the magnetic–mechanical coupling simulation is carried out to obtain the vibration characteristics of the core. The distribution of magnetic flux density and stress near the air gap and the corner of the core are indicated. The

Authorized licensed use limited to: Hebei University of Technology. Downloaded on September 12,2025 at 02:31:59 UTC from IEEE Xplore. Restrictions apply.

difference in magnetic flux density inside and outside the core is reduced due to the air gap. The contact stress between two U-shaped cores changes in a vibration period and reaches a maximum of 17.6k N/m^2. The maximum stress located in the corner is 24k N/m^2.

Finally, a measuring platform is built to measure the vibration velocity of the core under sinusoidal excitation. The magnetic properties and vibration characteristics are obtained. With the increase of magnetic flux density and frequency, the core loss increases and reaches 6.36 W/kg at 200 Hz and 1.6 T. The vibration intensity near the air gap and the corner is larger than the other locations, with a maximum of 2.4e^{-3} m/s at 200 Hz. With the increase of magnetic field intensity, more harmonics appear in magnetic flux density, which results in the vibration under twice the harmonic frequency. When the power frequency is far from the natural frequency of the core, the vibration frequency is twice the power frequency. When the harmonic frequency in the excitation or magnetic flux density coincides with the natural frequency of the core, mechanical resonance occurs, and the vibration of the core is greatly enhanced. Compared with the results of the simulation and experiment, the vibration near the air gap and the corner of the core is superior to other areas. The error is 8.76% for the point near the air gap and 8.96% for the point near the corner, which proves the homogenization method presented in this article can effectively calculate the vibration of the ASR core. The uncertainty of the measurement is analyzed and measures to improve the stability of the measurement results are proposed.

By investigating the vibration characteristics of the ASR core, a theoretical foundation has been laid for the structural design and fault detection of ASR. Meanwhile, the study is the basic to evaluate the long-term effects of these vibrations on the ASR's performance and reliability over time.

REFERENCES

[1] K. Liu, K. Li, Z. Chang, C. Fan, and S. Hu, "Research on losses and heat dissipation of saturable reactor used in converter valve," *IEEE Access*, vol. 10, pp. 17796–17802, 2022.

[2] Y. Song, J. Sun, M. Saeedifard, S. Ji, L. Zhu, and A. P. S. Meliopoulos, "Optimum selection of circuit breaker parameters based on analytical calculation of overcurrent and overvoltage in multiterminal HVDC grids," *IEEE Trans. Ind. Electron.*, vol. 67, no. 5, pp. 4133–4143, May 2020.

[3] Y. Dou, Y. Li, Z. Lin, S. Yue, and J. Zhu, "An improved cross-yoke SST for accurate 1-D and 2-D magnetic testing of Fe-SI sheets," *IEEE Trans. Instrum. Meas.*, vol. 71, 2022, Art. no. 6000210.

[4] P. Shuai and J. Biela, "Influence of material properties and geometric shape of magnetic cores on acoustic noise emission of medium-frequency transformers," *IEEE Trans. Power Electron.*, vol. 32, no. 10, pp. 7916–7931, Oct. 2017.

[5] Z. Chen, Q. Zhou, G. Ding, X. Wu, J. Wu, and Y. Zhang, "Influence of magnetic state variation on transformer core vibration characteristics and its measurement," *IEEE Trans. Instrum. Meas.*, vol. 71, 2022, Art. no. 6004108.

[6] B. Tong, Y. Qingxin, Y. Rongge, and Z. Lihua, "Magnetically controlled saturable reactor core vibration under practical working conditions," *IEEE Trans. Magn.*, vol. 53, no. 6, pp. 1–4, Jun. 2017.

[7] J. Zheng, H. Huang, and J. Pan, "Detection of winding faults based on a characterization of the nonlinear dynamics of transformers," *IEEE Trans. Instrum. Meas.*, vol. 68, no. 1, pp. 206–214, Jan. 2019.

[8] X. Zhou, X. Zhu, Z. Xiang, D. Fan, L. Xu, and T. Zhu, "Harmonic-oriented design and vibration characteristic suppression for interior permanent magnet motors," *IEEE Trans. Ind. Electron.*, vol. 71, no. 2, pp. 1246–1256, Feb. 2024.

[9] R. M. Pindoriya, R. K. Thakur, B. S. Rajpurohit, and R. Kumar, "Numerical and experimental analysis of torsional vibration and acoustic noise of PMSM coupled with DC generator," *IEEE Trans. Ind. Electron.*, vol. 69, no. 4, pp. 3345–3356, Apr. 2022.

[10] C. Peng, D. Wang, B. Wang, J. Li, C. Wang, and X. Wang, "Different rotor segmented approaches for electromagnetic vibration and acoustic noise mitigation in permanent magnet drive motor: A comparative study," *IEEE Trans. Ind. Electron.*, vol. 71, no. 2, pp. 1223–1233, Feb. 2024.

[11] A. Krings, A. Boglietti, A. Cavagnino, and S. Sprague, "Soft magnetic material status and trends in electric machines," *IEEE Trans. Ind. Electron.*, vol. 64, no. 3, pp. 2405–2414, Mar. 2017.

[12] C. Zhang, X. Yan, Y. Li, and Q. Yang, "Vector magnetic properties measurement of silicon steel under biased magnetic excitation along laminated direction," *IEEE Trans. Magn.*, vol. 55, no. 2, pp. 1–4, Feb. 2019.

[13] M. C. Guimarães, F. L. Alcântara, R. U. C. Moreira, N. E. F. Lima, and J. G. Ank, "Improvement of magnetic properties of a reversible hot rolled grain-oriented electrical steel," *IEEE Trans. Magn.*, vol. 52, no. 5, pp. 1–4, May 2016.

[14] S. Ito, T. Mifune, T. Matsuo, and C. Kaido, "Energy-based magnetization and magnetostriction modeling of grain-oriented silicon steel under vectorial excitations," *IEEE Trans. Magn.*, vol. 52, no. 5, pp. 1–4, May 2016.

[15] Y. Li, S. Wang, Y. Wu, Y. Jiang, Z. Xiao, and Y. Tang, "Heterogeneous integration of isotropic and anisotropic magnetic cores for inductive power transfer," *IEEE Trans. Power Electron.*, vol. 40, no. 2, pp. 3770–3784, Feb. 2025.

[16] S. Gao, C. Zhang, L. Zhou, T. Lin, X. Zhou, and J. Cai, "A homogeneous model for estimating eddy-current losses in wound core of multilevel-circle section," *IEEE Trans. Transport. Electrific.*, vol. 6, no. 2, pp. 752–761, Jun. 2020.

[17] J. Šarloši and J. Bocko, "Effective material moduli for composites," *Am. J. Mech. Eng.*, vol. 4, no. 7, pp. 289–292, 2016.

[18] Methods of Measurement of the Magnetostriction Characteristics of Grain-oriented Electrical Steel Strip and Sheet By Means of a Single Sheet Tester and an Optical Sensor, IEC Standard 60404-17, 2021.

[19] C. Zhang, Y. Li, J. Li, Q. Yang, and J. Zhu, "Measurement of three-dimensional magnetic properties with feedback control and harmonic compensation," *IEEE Trans. Ind. Electron.*, vol. 64, no. 3, pp. 2476–2485, Mar. 2017.

[20] Metallic Materials—Tensile Testing—Part 1: Method of Test at Room Temperature, ISO Standard 6892-1, 2019.

[21] Standard Test Method for Young's Modulus, Tangent Modulus, and Chord Modulus, Standard ASTM Standard E111-17, 2017.

[22] S. Tan, J. Lu, X. Zhang, B. Li, Y. Zhang, and Y. Jiang, "The numerical analysis methods of electromagnetic rail launcher with motion," *IEEE Trans. Plasma Sci.*, vol. 44, no. 12, pp. 3417–3423, Dec. 2016.

[23] H. Wang, L. Qu, W. Qiao, and B. Liu, "Magnetic flux valve: A magnetoelectric materials-based device for conversion and control of electric power," *IEEE Trans. Ind. Electron.*, vol. 64, no. 3, pp. 2451–2458, Mar. 2017.

[24] J. Chen, D. Wang, S. Cheng, Y. Wang, Y. Zhu, and Q. Liu, "Modeling of temperature effects on magnetic property of nonoriented silicon steel lamination," *IEEE Trans. Magn.*, vol. 51, no. 11, pp. 1–4, Nov. 2015.

[25] K. Kume, R. Inoue, H. Ueda, and S. Kim, "Study on the magnetic properties of metal substrates at low temperature by fabricated compact SST," *IEEE Trans. Appl. Supercond.*, vol. 32, no. 6, pp. 1–4, Sep. 2022.



Tao Chen was born in Shandong, China, in 1997. He received the B.E. degree from the Qilu University of Technology (Shandong Academy of Sciences), Jinan, China, in 2019. He is currently pursuing the master's and Ph.D. degrees in electrical engineering with Hebei University of Technology, Tianjin, China.

His research interests include the measurement of magnetic properties and magnetostrictive properties, the calculation and measurement of vibration, and acoustic noise of high-frequency transformer.

Authorized licensed use limited to: Hebei University of Technology. Downloaded on September 12,2025 at 02:31:59 UTC from IEEE Xplore. Restrictions apply.



Qingxin Yang received the B.S., M.S., and Ph.D. degrees in electrical engineering from Hebei University of Technology, Tianjin, China, in 1983, 1986, and 1997, respectively.

Since 1996, he has been a Professor with Hebei University of Technology. From 2008 to 2018, he was the President with Tianjin Polytechnic University, Tianjin. He is currently with Tianjin University of Technology, Tianjin, where he was the President from 2018 to 2020. His research interests include computational electromagnetism, wireless power transfer, and engineering electromagnetism applications.

Dr. Yang was a Board Member of the International Compumag Society and the President of China Chapter. Since 2015, he has been the President of China Electrotechnical Society.



Changgeng Zhang was born in Heilongjiang, China, in 1985. He received the B.E. degree from Tianjin Polytechnic University, Tianjin, China, in 2009, the M.S. degree from Nankai University, Tianjin, in 2012, and the Ph.D. degree from Hebei University of Technology, Tianjin, in 2017.

From December 2018 to December 2019, he was a Visiting Scholar with Ohio State University, Columbus, OH, USA. He is currently a Full Professor with the Electrical Engineering School, Hebei University of Technology. His research interests include magnetic properties measurement, finite element analysis, and modeling of magnetic materials.



Yongjian Li was born in Hebei, China, in 1978. He received the B.Eng., M.Eng., and Ph.D. degrees in electrical engineering from Hebei University of Technology, Tianjin, China, in 2002, 2007, and 2011, respectively.

From 2009 to 2011, he was a Research Assistant with the University of Technology Sydney, Ultimo, NSW, Australia. From 2016 to 2017, he visited Ottawa University, Ottawa, ON, Canada, as a Visiting Scholar. Since 2015, he has been a Full Professor with the Electrical Engineering School, Hebei University of Technology. His research interests include computational electromagnetics, measurements, and modeling of magnetic properties, and high-frequency transformers.



Yu Dou was born in Heilongjiang, China, in 1995. He received the B.E. degree in electrical engineering and automation from Harbin University of Science and Technology, Harbin, China, in 2017. He is currently pursuing the M.E. and Ph.D. degrees in electrical engineering with Hebei University of Technology, Tianjin, China.

He is currently a Post-Doctoral Researcher with Zhejiang University, Haining, China. His current research interests include magnetic domain imaging and measurement of magnetic properties.



Shuaichao Yue was born in Hebei, China, in 1992. He received the B.Eng., M.Eng., and Ph.D. degrees in electrical engineering from Hebei University of Technology, Tianjin, China, in 2016, 2018, and 2023, respectively.

From 2019 to 2021, he was a Visiting Researcher at Wolfson Centre for Magnetics, Cardiff University, Cardiff, U.K. He is currently a Post-Doctoral Researcher with Hebei University of Technology. His research interests include the measurement of magnetic properties and hysteresis modeling and its application.

Authorized licensed use limited to: Hebei University of Technology. Downloaded on September 12,2025 at 02:31:59 UTC from IEEE Xplore. Restrictions apply.